Journal Name

ARTICLE

Formation of calcium phosphate nanostructures under the influence of self-assembling hybrid elastin-like-statherin recombinamers

Received 00th January 20xx,
Accepted 00th January 20xx

DOI: 10.1039/x0xx00000x

www.rsc.org/

M. Hamed Misbah,[a] M. Espanol,[b] Luis Quintanilla,[a] M. P. Ginebra[b] and J. Carlos Rodríguez-Cabello*[a]

The self-assembling properties of thermally-sensitive amphiphilic elastin-like multiblock recombinamers have been combined with the capacities of calcium phosphate binding of the SN_A15 epitope inspired by the salivary protein statherin. In this regard, the interaction between calcium and phosphate ions was examined in the presence of two hybrid recombinamers. The first recombinamer comprised a simple amphiphilic diblock in which the SN_A15 epitopes were combined, at the gene level, to the hydrophilic end. This recombinamer can self-assemble into nanoparticles that can control the transformation of amorphous calcium phosphate (ACP) into fibre-like hydroxyapatite structure. In the other recombinamer, the SN_A15 domains are distributed along monomer chain, with the hydrophilic blocks being distributed amongst the hydrophobic ones. In this case, the resulting nanohybrid ACP/recombinamer organises into neuron-like structures. Thus, combining the amphiphilic elastin-like recombinamers to the SN_A15 functionality is a powerful mean to tune the formation of different complex calcium phosphate nanostructures.

1. Introduction

The synthesis of self-assembled calcium phosphate hybrid structures represents a novel approach for the fabrication a new class of materials. In self-assembly processes, non-covalent cooperative interactions are responsible for the aggregation and formation of supramolecular structures with unique properties.[1-3] In the particular field of calcium phosphates, self-assembly represents a major tool for understanding bone mineralization and the basis to create new functional materials. In this process, organic molecules with different amphiphilic properties regulate the organization of different organic/inorganic hybrid structures, thus controlling the biomimetic mineralization process.[1, 2, 4, 5] They can be introduced as insoluble additive (templating approach) like is the case of Langmuir monolayers and self-assembled monolayers that are used to determine the functional group distance to nucleate a desired mineral phase or even to control the growth of particular polymorphs.[4, 6-8] Alternatively, organic molecules can also be used as soluble additives imparting great influence on crystallization modulating the morphology, size and polymorph type of the crystal.[4, 9, 10] The ability of organic molecules to complex ions, self-aggregate or adsorb onto specific crystal surfaces are just some strategies through which soluble molecules control mineralization.

Various types of organic molecules have been used to investigate the organization of the organic/inorganic hybrid structures, to help understanding the mechanisms controlling the biomimetic mineralization processes.[1, 2, 4, 5] For example, self-assembled peptide-amphiphile can direct hydroxyapatite (HA) to form a composite material with an organization similar to that found for collagen fibrils and HA in bone.[1, 2] Furthermore, diblock copolymers can induce meso-skeleton formation of interconnected calcium phosphate nanofibers with a star/neuron-like morphology, although more complex nested forms can also be produced.[2, 5] Identical structures have also been generated using simpler organic molecules such as surfactants, sodium polyacrylate and poly (diallyldimethylammonium chloride).[9] Also, studies using dephosphorylated Fluorenylmethyloxycarbonyl (Fmoc) tyrosine phosphate had demonstrated the capability of spontaneously forming fibers that could later be mineralized.[11]

Elastin-like polypeptides and, now-a-days, their recombinant versions, elastin-like recombinamers (ELRs) are a family of polypeptides inspired by natural elastin that can be used to control the biomimetic mineralization process.[12] They are composed of simple amino-acid

[a] G.I.R. Bioforge, University of Valladolid, CIBER-BBN, Paseo de Belén 19, 47011 Valladolid, Spain.
[b] Biomaterials, Biomechanics and Tissue Engineering Group, Department of Materials Science and Metallurgy, Technical University of Catalonia, Diagonal 647, 08028 Barcelona, Spain.
* Corespondng author, E-mail: roca@bioforge.uva.es
Electronic Supplementary Information (ESI) available: Elastin-like recombinamer characterization and additional experimental data are included. See DOI: 10.1039/x0xx00000x

sequences (VPGXG)* (see Table 1 for details on sample nomenclature), where X can be any natural or synthetic amino acid except proline.[13-15] In aqueous solution, ELRs exhibit an intrinsic inverse transition temperature (T_t). Below T_t, the free chains remain disordered and have random coil conformations that are fully hydrated as a result of hydrophobic hydration. This hydration around hydrophobic moieties is ordered into cage-like or clathrate structures that are stabilized by hydrogen bonding. In contrast, above T_t the ELR backbone is dehydrated and can self-assemble into β-turn conformations.[13-15] In this structure, intra- and inter-chain hydrophobic contacts result in formation of a phase-separated state. The guest amino acid residue (X) can be varied to change the value of T_t and, consequently, the amphiphilic properties of the designed ELR block.[13, 16] For example, poly(VPGIG) exhibits a hydrophobic nature stemming from the presence of L-isoleucine (I) as guest.[16, 17] In contrast, poly(VPGEG) and poly(VPGKG) exhibit a hydrophilic nature due to the presence of L-glutamic (E) acid and L-lysine (K), respectively.[16, 18]

The above simple ELR-based blocks can be combined with each other to make amphiphilic ELRs that can self-assemble and generate different nanostructures.[3, 19] For example, the ELR E50I60 is composed of an I60 block ($(VGIPG)_{60}V$) with a T_t of about 19 °C and an E50 block ($MESLLP((VPGVG)_2(VPGEG)(VPGVG)_2))_{10}$) whose estimated T_t is higher than 100 °C at neutral pH.[3, 18, 20] The chains of this ELR can self-assemble into micelles in which the hydrophobic I60 blocks form the core and the hydrophilic E50 blocks the corona. In contrast, the ELR IK24 ($MESLLP[[(VPGIG)_2(VPGKG)(VPGIG)_2]_{24}V$) cannot form a micellar structure above its T_t of 31.5 °C.[19] The chain of this ELR is composed of hydrophobic $(VPGIG)_2$ and hydrophilic (VPGKG) blocks.[19]

Such biocompatible ELRs could be used as a regenerative material in various applications, such as bone regeneration, when recombined with a bioactive domain.[12] This domain could, for example, be the hydrated N-terminal 15-amino-acid residue of salivary statherin known as SN15 ($DS_PS_PEEKFLRRIGRFG$), or its analog SN_A15 (DDDEEKFLRRIGRFG).[21] Due to their charge density and helical conformation, these proteins domains exhibit a high affinity for calcium phosphate and therefore high adsorption on the surface of HA.

The main goals of the present work were to study the influence of SN_A15 on the behavior of calcium phosphate interaction when incorporated into ELR and to elucidate how the amphiphilic properties of these ELRs affect the calcium phosphate phases and morphologies generated. To this end, new hybrid recombinamer was designed, produced and characterized in which three SN_A15 domains were combined with the hydrophilic end of the ELR E50I60, thus resulting in the presence of SN_A15 on the external surface of E50I60 micelles. The effect of this ELR on calcium phosphate formations was studied in parallel with that of the ELR ((IK)2-SN_A15-(IK)2)3, which has three SN_A15 domains distributed along its monomer chain.

2. Materials and experimental methods

2.1. Recombinamer synthesis

The composition and length of monodiperse amphiphilic ELR molecule can be controlled using standard genetic engineering methods.[22] As such, sequential introduction of repetitive EL- or SN_A15-polypeptide-coding gene segments was carried out using the recursive directional ligation technique to form fusion genes. This method requires the construction of coding gene segments flanked at both ends with non-palindromic restriction sites. In this work, the gene segments encoding each monomer were contained in a modified version of the cloning vector pDrive (Qiagen), known as pDAll, which is characterized by the engineering of two inverted Ear I and one Sap I restriction sites into the poly-linker region. Construction of the $(SN_A15)_3E50I60$ sequence was verified using agarose gel electrophoresis of the restriction fragments generated after enzymatic digestion and automated DNA sequencing. Selected genes were sub-cloned into a modified version of pET-25(+) expression vector and then transformed into *E. coli* strain BLR (DE3) star (Invitrogen).

2.2. ELR production and purification

Purification was performed by inverse temperature cycling using the following procedures.[22] After lysis of *E. coli* expression colonies, the denatured materials were removed by cold centrifugation (4 °C) at 15000 × g for 30 min. After that, 1 M of NaCl was added to the soluble fraction and the mixture heated for 1 h at 40 °C. Centrifugation at 40 °C was performed, and the insoluble fraction was re-suspended in cold ultrapure water, followed by cold centrifugation. The soluble fraction was subjected to two additional cycles of heating with NaCl addition and cold re-suspension. Finally, the ELR was dialyzed in ultrapure water and the final pH of the solution adjusted to about 7.4, followed by lyophilization. The resulting $(SN_A15)_3E50I60$ was characterized by matrix-assisted laser desorption-ionization time-of-flight (MALDI-TOF) mass spectrometry, amino-acid analysis, nuclear magnetic resonance (NMR), attenuated total reflection infrared (ATR-IR) spectroscopy and differential scanning calorimetery (DSC).

2.3. MALDI-TOF mass Spectrometry

MALDI-TOF mass spectrometry was used to determine the molecular weight of ELRs. The matrix used for MALDI-TOF analysis was composed of 7.6 mg of 2,5-DHAP dissolved in 375 µL of ethanol and mixed with 125 µL of 18 mg/mL $C_6H_8O_7{\cdot}2NH_3$ aqueous solution. Then, 1 µL from this matrix was added to the MALDI plate along with 1 µL ELR solution. The plate was dried in air and the mass

spectra collected using a Bruker autoflex speed instrument equipped with a nitrogen laser (337 nm) operating in the positive ion mode with delayed extraction.

2.4. NMR spectroscopy

Proton nuclear magnetic resonance (^{1}H NMR) spectroscopy was performed using a 400-MR NMR spectrometer (400 MHz, Agilent Technologies). 15-20 mg of the purified ELR was dissolved in 600 µL of deuterated dimethyl sulfoxide (DMSO-d_6) and the spectrum measured at 25 °C. Chemical shifts (δ) are given in ppm. Data were processed using MestReNova software. DMSO-d_5 peaks at δ = 2.5 ppm was used as internal reference for the ^{1}H spectra.

2.5. Amino acid Analysis

Samples were hydrolysed in 6 M HCl and 2% Phenol (30 min at 160 °C) and evaporated under inert atmosphere. The solid residues were re-suspended in 1 mL of 0.1 M HCl. Then, derivatizations with the OPA and FMOC chemistries were performed using an Agilent 1329A auto-sampler as reported in literature.[23] The derivatized amino acids were analysed by HPLC with UV detection using an Agilent 1200 series variable wavelength detector equipped with a G1314B detector.

2.6. ATR-IR Spectroscopy

ATR-IR analyses were conducted using a BRUKER TENSOR 27, USA spectrophotometer. Solid ELR samples were placed directly on the ATR crystal for measurement. For each spectrum, a 128-scan was collected with a resolution of 2 cm^{-1} in the range 4000 to 600 cm^{-1}. Spectral manipulations were performed using the OPUS (version 4.2) software (MATTSON INSTRUMENT, INC.).

2.7. DSC

A Mettler Toledo 822e differential scanning calorimeter (DSC), with liquid-nitrogen cooler and calibrated with indium, was used to calculate the T_t of the ELRs synthesized. ELR samples were dissolved in ultrapure water at a concentration of 50 mg/mL at 4 °C. Then, 20 µL of ELR solution was placed in a 40 µL sealed aluminum pan, and the same volume of ultrapure water was placed in the reference pan. Before the experiment, samples were held at 0 °C for 5 min and measurements were performed in the range 0 to 60 °C at a heating rate of 5 °C/min.

2.8. Circular dichroism (CD)

A Jasco J-815 spectropolarimeter (Jasco Inc., Easton, MD) under a constant nitrogen gas flow was used to obtain CD spectra for ELRs. Samples were dissolved in 0.5 mM $CaCl_2$ (pH ~ 7.4) at 0.05 mg/mL, and filtered using a PVDF 0.45µm STE: R syringe filter at 4 °C. CD spectra were recorded at 37 °C over the wavelength range 190-260 nm, using a 0.2-cm path length quartz cell, recording a point every 0.5 nm with a scan speed of 50 nm/min.

2.9. Calcium phosphate precipitation in the presence of ELRs

When a solution of calcium cations is mixed with a solution of phosphate anions, calcium phosphate nucleation and crystallization can take place. To be able to investigate the effect of various ELRs on the reaction of calcium phosphate, the following procedure was performed. The first step was to dissolve ELR at the desired concentration in 10 mM solution of $CaCl_2$ at 4 °C. The sample solution was then heated to 37 °C and kept at this temperature for least 15 min (pH 7.4) under continuous magnetic stirring. After that, an equivolume solution of 6 mM Na_2HPO_4 at 37 °C (pH 7.4) was added to the solution to give a final Ca/P ratio of 1.67, similar to that found in the literature.[6, 9] The calcium phosphate precipitation was studied at final ELRs concentrations of 0, 0.5, 1, 2, 3 and 4 mg/mL. All reagents used for preparation of calcium and phosphate solutions were obtained from Sigma Aldrich and used without further purification. The temperature was controlled during the reaction using thermo-jacketed vessels coupled to a thermostatic bath (Huber CC2).

The calcium phosphate reaction was monitored with the help of an electrical conductivity probe (Crison MM41). The initial time of reaction (t = 0) was taken when the phosphate solution added to the mixture. All conductivity profiles were analyzed and the induction time, defined as the time taken for metastable transient phases to transform into more stable phases, was determined.[9, 24]

2.10. X-ray diffraction (XRD):

The composition of calcium phosphate precipitated in the absence or presence of ELRs were analyzed by X-ray diffraction. Samples were isolated by centrifugation, washed two times using ultrapure water and dried at 37 °C. The white precipitate was then ground in an agate mortar prior to XRD analysis. XRD patterns were recorded on a Bruker D8 Discover A 25 equipment using CuK_α radiation (λ = 1.5406 Å) and a silicon sample holder. The step size was 0.02°. Crystallographic identification of the examined phases was compared with the PDF 01-072-1243.

2.11. Energy dispersive X-ray spectroscopy (EDX):

The Ca/P ratio of the calcium phosphate precipitated after centrifugation, washing and drying, were determined by energy dispersive X-ray spectroscopy (EDAX Genesis with an Apollo SDD detector, 10 mm).

Table 1. Amino acid sequence of the ELRs.

ELR name	ELR amino acid sequence*	Mw (kDa)
E50I60	MESLLP[((VPGVG)$_2$(VPGEG)(VPGVG)$_2$)$_{10}$](VGIPG)$_{60}$V	46999±19.96
(SN$_A$15)$_3$E50I60	MESLLPV(DDDEEKFLRRIGRFG)3[((VPGVG)$_2$(VPGEG)(VPGVG)$_2$)$_{10}$](VGIPG)$_{60}$V	52970 ±12
(IK)24	MESLLP[[(VPGIG)$_2$(VPGKG)(VPGIG)$_2$]$_{24}$V	51996.5±11.30
((IK)2-SN$_A$15-(IK)2)3	MESLLP[[(VPGIG)$_2$(VPGKG)(VPGIG)$_2$]$_2$DDDEEKFLRRIGRFG[(VPGIG)2(VPGKG)(VPGIG)$_2$]$_2$]$_3$V	31857

* D= L-aspartic, E= L-glutamic, K= L-lysine, F= L-phenylalanine, L= L-leucine, R= L-arginine, I= L-isoleucine, G= Glycine, V= L-valine, P= L-proline, M= L-methionine and S= L-serine.

2.12. Transmission electron microscopy (TEM)

TEM specimens were prepared by soaking a 300 mesh carbon-coated copper grid in the required solution for the required time. The grid was then removed and blotted immediately to remove the excess of liquid, and air-dried. Electron microscopy and diffraction were performed using a JEOL-JEM 2200FS system operating at 200 kV and equipped with an energy dispersive X-ray (EDX) analysis detector. The microscope was equipped with an in-column Ω-type energy filter. Zero-loss images were recorded to increase contrast. X-ray spectra were acquired in scanning transmission electron microscopy (STEM) mode using an Oxford INCA EDX system. The live counting time was 100 s.

3. Results and discussion

Hybrid elastin-like-statherin recombinamers

The amino acid sequence of the different constructs E50I60, (SN$_A$15)$_3$E50I60, IK24 and ((IK)2-SN$_A$15-(IK)2)3 are shown in Table 1. E50I60, (IK)24 and ((IK)2-SN$_A$15-(IK)2)3 were synthesized and characterized as reported previously in the literature.[19, 20, 25] The transition temperature (T_t) of the ELR E50I60 was exploited to purify the whole (SN$_A$15)$_3$E50I60 hybrid molecule under water-based and mild conditions. The final (SN$_A$15)$_3$E50I60 product was characterized by SDS-page analysis, MALDI-TOF mass spectrometry, ^{1}H NMR, amino-acid analysis and ATR-IR spectroscopy (Supplementary information: Figures S1-S4 and Table S1-S2), which proven the correctness and purity of the biosynthetic process in terms of sequence and molecular mass. DSC experiments were performed in order to check the T_t of the ELR (SN$_A$15)$_3$E50I60 (Figure S5).

As the secondary structure of polypeptides has a remarkable influence on controlling the mineralization process,[4, 10, 26] CD was used as a spectroscopic technique to study the conformation of ELRs shown in Table 1. Calcium phosphate interaction in the presence of these ELRs was then examined by monitoring the electrical conductivity (σ) as a function of time. The induction time (I_t), defined as the time at which a stable solid phase starts to form, was also determined. The formed calcium phosphates were characterized by XRD. Moreover, the morphologies of the calcium phosphate species formed were observed by TEM and characterized by electron diffraction and EDX. To this end, the reaction conditions were chosen carefully to be able to visualize the amorphous phase transformations in an adequate time frame.

Circular dichroism spectroscopy (CD)

CD has been used to analyze the basic secondary structure of polypeptide, α-helix, β-sheet, β-turns and random coils.[27-30] Figure 1 shows the CD spectra recorded for the ELRs, all of which exhibit one positive and two negative peaks. The negative peaks centered at 197, 199 and 200.5 nm are attributed to the random coil conformations, whereas the negative peak centered at 223 nm and the positive peak at 209-212 nm are assigned to type II β-turns.[28-30] The Mean Residual Ellipticity (MRE) of the characteristic random coil peak of these ELRs is higher than that found for an ideal random coil (-40000 deg·cm^2·dmol^{-1}).[29, 30] This is due to the presence of β-turn conformations stemming from the hydrophobic (VPGIG) block.

Figure 1A shows that the center of the random coil peak is shifted from 197 to 199 nm, with its amplitude changing from -3670 to -3463 deg·cm^2·dmol^{-1} when SN$_A$15 is recombined with the E50I60 monomer chain. In addition, the amplitude of the β-turn peak alters from -2581 to -3019 deg·cm^2·dmol^{-1}. A similar behavior can be observed in Figure 1B for IK24 and ((IK)2-SN$_A$15-(IK)2)3 in which the characteristic random coil peaks are found at 197 and 200.5 nm with MRE amplitudes of -6421 and -4436 deg·cm^2·dmol^{-1}, respectively. There is no shift in the amplitude of the β-turn peak can be seen.

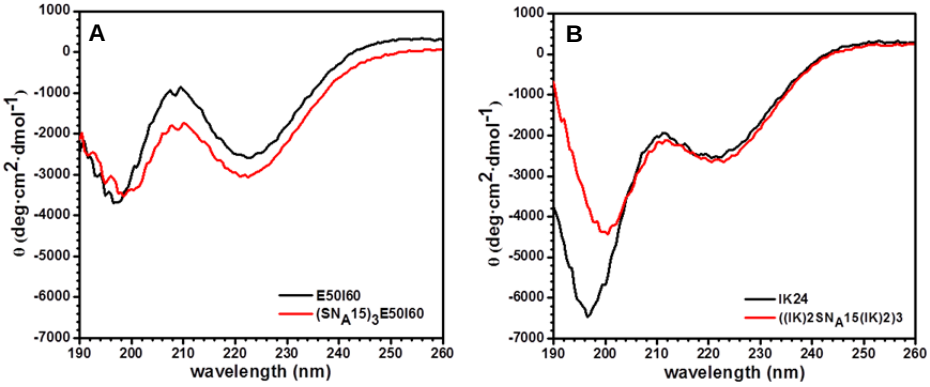

Figure 1. CD of ELRs at 0.05 mg/mL dissolved in 0.5 mM $CaCl_2$ (37 °C), (A) E50I60 and $(SN_A15)_3$E50I60, and (B) IK24 and ((IK)2-SN_A15-(IK)2)3.

Formation of nanofibre-like hydroxyapatite structure controlled by $(SN_A15)_3$E50I60

Electrical conductivity measurements performed during the calcium phosphate reaction in the absence/presence of E50I60 and $(SN_A15)_3$E50I60 are shown in Figure 2A. The profiles presented clearly exhibit three regions after phosphate addition. Region I corresponds to the initial precipitation of a metastable calcium phosphate phase, which is an amorphous phase that is susceptible to rapid transformation (region II) into a secondary stable precipitate (region III).[9, 24] It can be seen from Figure 2B that E50I60 does not significantly affect the I_t, which remains at about 5 min, even with increasing concentration. This value is similar to that obtained for the control sample in the absence of ELRs. In contrast, $(SN_A15)_3$E50I60 delays the secondary precipitation with a nearly constant I_t of around 25 min.

The precipitates formed after I_t (region III) were examined using XRD (Figure 2C) confirming the presence of HA (PDF 01-072-1243). The peaks are broad accounting for the poorly crystalline nature of the precipitates. The Ca/P ratio of the precipitates in the presence of 2 mg/mL E50I60 and $(SN_A15)_3$E50I60 were 1.45 ± 0.02 and 1.46 ± 0.02, respectively, and that of HA formed in the absence of ELRs was 1.45 ± 0.02. These ratios are assigned to calcium deficient HA.[31-33]

The morphologies and phases of the formed calcium phosphate after I_t (region III) are shown in Figure 3. In the absence of ELRs, the formed calcium phosphate is mostly composed of plate-like crystals, as shown in Figure 3A. Moreover, the electron-diffraction pattern shown in the inset to the figure exhibits a crystal lattice corresponding to the HA phase consistent with the XRD results. The addition of E50I60 does not seem to significantly alter the morphology of the HA (Figure 3B), whereas a completely different structure consisting of polycrystalline nanofibre-like HA aggregates (Figure 3C) is formed in the presence of $(SN_A15)_3$E50I60.

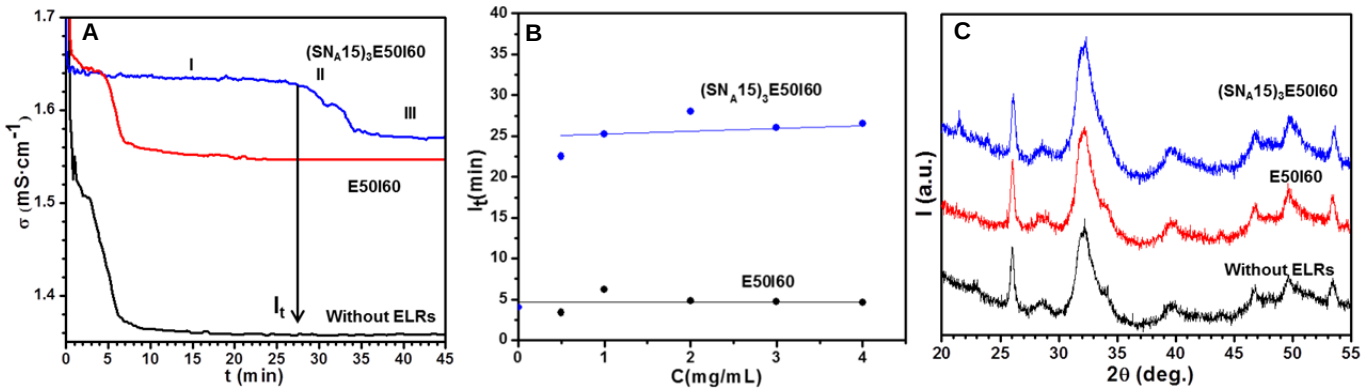

Figure 2. (A) Electrical conductivity profiles measured by mixing 3 mL of 10 mM $CaCl_2$ and 3 mL of 6 mM Na_2HPO_4 at 37 °C (pH 7.4) in the presence of E50I60 (red curve) and $(SN_A15)_3$E50I60 (blue curve) at 2 mg/mL. The conductivity profile (black curve) in the absence of these ELRs is included for comparison. (B) I_t as a function of these ELR concentrations. Lines are drawn to allow the changes to be seen more clearly. (C) XRD patterns of the precipitates after I_t (region III) in the presence of E50I60 (red curve) and $(SN_A15)_3$E50I60 (blue curve) at 2 mg/mL. The XRD pattern of the precipitate formed in the absence of ELRs (black curve) is included for comparison.

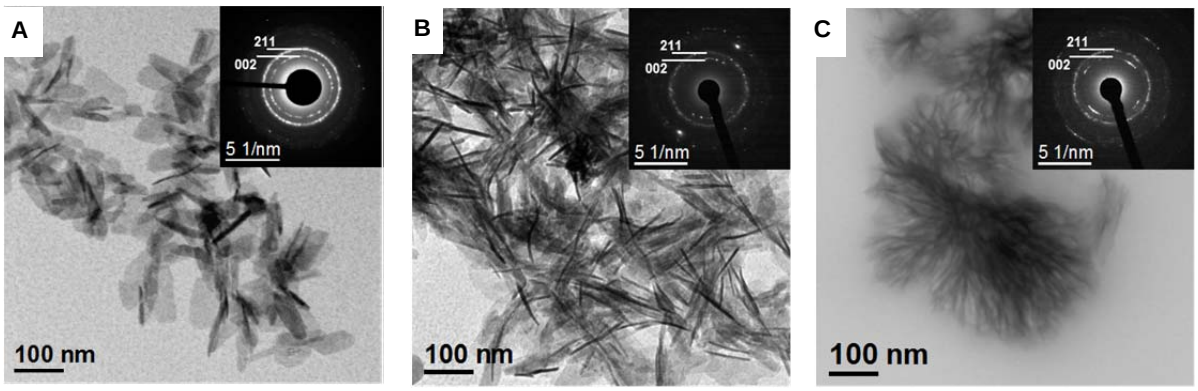

Figure 3. TEM showing the morphology of the calcium phosphate obtained after I_t and their corresponding electron-diffraction patterns: (A) in the absence of ELRs and in the presence of (B) 2 mg/mL E50I60 and (C) 2 mg/mL $(SN_A15)_3$E50I60. Some planes consistent with the HA crystal lattice can be observed in the electron-diffraction patterns (inset).

Formation of neuron-like morphologies controlled by ((IK)2-SN_A15-(IK)2)3

Figure 4A shows the electrical conductivity profiles for the mixed calcium phosphate solutions in the absence/presence of (IK)24 and ((IK)2-SN_A15-(IK)2)3. Figure 4B shows that I_t is independent of the presence of the former ELR, remaining at about 5 min even upon increasing the concentration. In contrast, the latter ELR delays secondary precipitation with a steady, concentration-dependent, increase in I_t up to about 37 min at 4 mg/mL. The XRD patterns (Figure 4C) of the precipitates formed in the absence/presence of (IK)24 and ((IK)2-SN_A15-(IK)2)3 are assigned to poorly crystalline HA phase (PDF 01-072-1243). The Ca/P ratio determined by EDX in the presence of 2 mg/mL of (IK)24 and ((IK)2-SN_A15-(IK)2)3 is 1.43 ± 0.02 and 1.47 ± 0.08 respectively, which is attributed to calcium deficient HA.[31-33]

Figure 5A shows the morphologies and phases of the calcium phosphate formed in the presence of IK24, confirming the formation of plate-like HA crystals similar to those observed in the control sample without ELRs. In contrast, for ((IK)2-SN_A15-(IK)2)3 neuron-like structures were mostly observed (Figures 5C, 5D). The cores of these neurons were examined by EDX revealing the presence of calcium and phosphate with Ca/P ~1.14 (Figures S6). At a concentration of 0.5 mg/mL, the neuron-like morphology has a core of about 40-50 nm and thin nanofilaments about 5-10 nm in width and 150-200 nm in length. Upon increasing the concentration to 2 mg/mL, the filaments become shorter (about 100-150 nm) whereas the core becomes larger (about 90-120 nm), thus forming a mesostructured ACP/((IK)2-SN_A15-(IK)2)3. High resolution TEM analyses demonstrate that the cores and filaments do not exhibit any crystallite formation. Electron-diffraction analyses of the neuron-like cores confirm their amorphous structure (inset of Figure 5C). This contrasts with the XRD patterns that indicate the presence of an additional phase: poorly crystalline HA. The presence of this phase is due to spontaneous precipitation and is not controlled by ((IK)2-SN_A15-(IK)2)3.

Although the self-assembling process of hybrid biomaterials in the present work has the merit of mild reaction conditions, the main disadvantage associated to this synthesis route is precisely the low temperature and the mild reaction conditions that often leads to precipitation of secondary phases (i.e. HA). Many alternative routes can be used to overcome this drawback (hydrothermal, sonochemical or combustion techniques among others) but at the cost of sacrificing the mild reaction conditions inherent to biomimetic synthesis routes.[32, 33] However, in spite of the presence of HA for ((IK)2-SN_A15-(IK)2)3, the effect of this recombinamer in the modulation of calcium phosphate precipitation is clear.

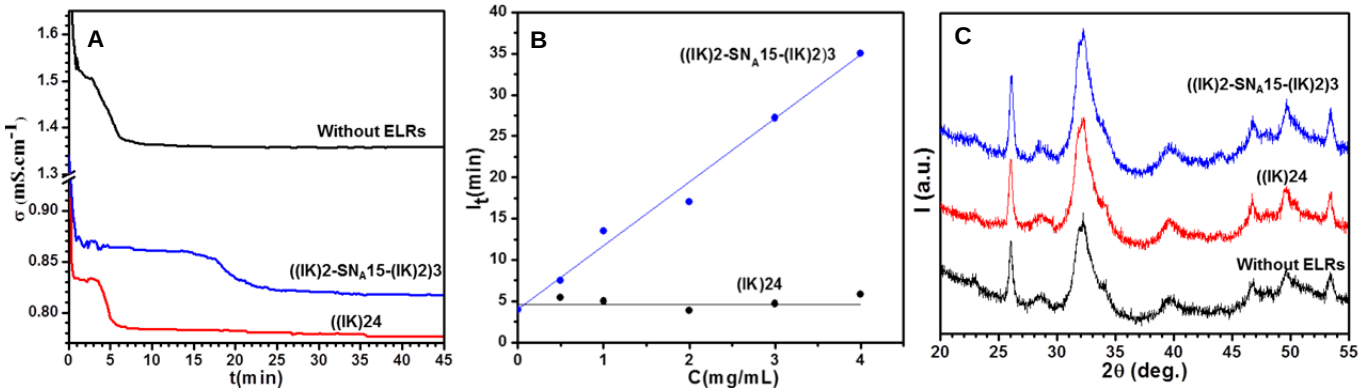

Figure 4. (A) Electrical conductivity profiles measured by mixing 3 mL of 10 mM $CaCl_2$ and 3 mL of 6 mM Na_2HPO_4 at 37 °C (pH 7.4) in the presence of IK24 (red curve) and ((IK)2-SN_A15-(IK)2)3 (blue curve) at 2 mg/mL. The conductivity profile (black curve) in the absence of these ELRs is included for comparison. (B) I_t as a function of IK24 and ((IK)2-SN_A15-(IK)2)3 concentration. Lines are drawn to allow the changes to be seen more clearly. (C) XRD patterns of the precipitates after I_t (region III) in the presence of IK24 (red curve) and ((IK)2-SN_A15-(IK)2)3 (blue curve) at 2 mg/mL. The XRD pattern of the precipitate formed in the absence of ELRs (black curve) is included for comparison.

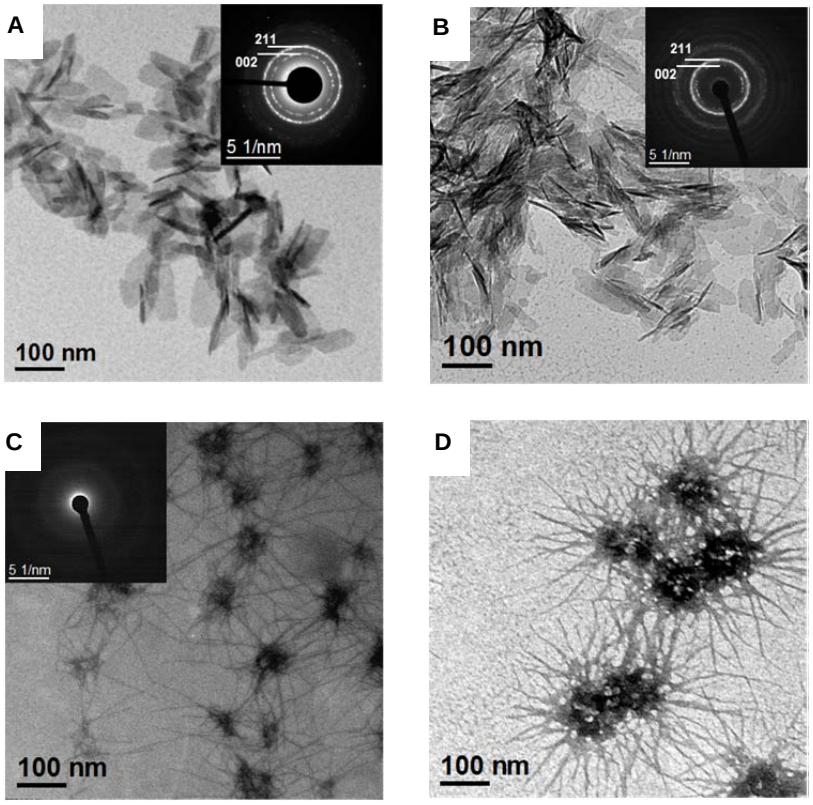

Figure 5. TEM showing the morphology of the calcium phosphate obtained after I_t (region III) and their corresponding electron-diffraction patterns: (A) in the absence of ELRs and in the presence of (B) 0.5 mg/mL (IK)24, (C) 0.5 mg/mL ((IK)2-SN_A15-(IK)2)3, and (D) 2 mg/mL ((IK)2-SN_A15-(IK)2)3.

Mechanisms controlling calcium phosphate formation under the influence of self-assembling ELRs as organic additives

Organic additives are well known to modulate amorphous-to-crystalline calcium phosphate transformations and to influence the stabilization of amorphous phases.[1, 2, 5, 6, 9, 34, 35] This can be achieved by the presence of locally highly charged areas on the organic molecules that can induce electrostatic and hydrogen-bonding interactions with the calcium and phosphate ions during the mineralization process. The hydrophobic constituent of these organic matrixes can act as an architectural framework, whereas the hydrophilic

constituents are directly involved in controlling mineral nucleation and growth. Due to the strong binding interactions between organic and inorganic phases, aggregates composed of hybrid primary particles with metastable ACP can be generated.[1, 2, 5, 6, 9, 34, 35] This metastable ACP can slowly crystallize inside these aggregates. For example, in the present work, the organic additives $(SN_A15)_3E50I60$ and ((IK)2-SN_A15-(IK)2)3 can delay I_t, whereas the other organic additives E50I60 and ((IK)24 cannot. Consequently, SN_A15 has a marked ability to control the mineralization process of calcium phosphate. Moreover, two different morphologies, namely fibre- and neuron-like structures, can be generated. These unexpected results can be interpreted on the basis of the interaction mechanisms that control ACP/ELR hybrid aggregate formation as a function of the amphiphilic properties of the ELR.

In the absence of ELRs, the mixing of calcium and phosphate solutions results in the formation of aggregated ACP spheres prior to I_t (Figure S7A), which are subsequently transformed into plate-like crystals after I_t (Figure 3A). In contrast, a dispersed hybrid spherical structure is formed in the presence of $(SN_A15)_3E50I60$ and ((IK)2-SN_A15-(IK)2)3 (Figures S7B, S7C). In consequence, flocculation bridging is prevented and the transformation dynamics are severely reduced. The formation mechanisms of these hybrid structures, and their transformation into different nanostructures, can be explained in detail using the schematic representations shown in Figures 6 and 7. Thus, $(SN_A15)_3E50I60$ can self-assemble into a micellar structure in which the $(SN_A15)_3$ domains are exposed on the outer surface (Figure 6A). This could explain why I_t remains practically the same regardless of $(SN_A15)_3E50I60$ concentration, thus meaning that calcium ions are readily sequestered by the $(SN_A15)_3$ and influencing any subsequent precipitation. The high density of negative charge concentrated on the micelle surface captures calcium ions, thereby generating a positive charge on the surface. Once the phosphate solution is added (before I_t), there are two possible pathways that the reaction mechanism can follow to generate the hybrid $(SN_A15)_3E50I60$/ACP structure. Firstly, the positively charged surface of the micelle (Figure 6A) can bind negatively charged phosphate groups and then, in turn, additional calcium ions, etc., thus resulting in the formation of ACP (Figure 6B). Secondly, $(SN_A15)_3E50I60$ micelles can be adsorbed onto the ACP surfaces formed, once the phosphate solution is added, via $(SN_A15)_3$ (Figure 6C). This would result in the formation of a dispersed hybrid spherical structure, as shown in supporting information Figure S6B. SN_A15 plays an important role in controlling the ACP transformation in both pathways, which can lead to preferential growth inhibition for different crystal phases by lowering their surface energy.[2] The hydrophilic $(SN_A15)_3E50$ segments are involved in controlling the transformation of ACP spheres into fibre-like HA (Figures 6D, 6E), whereas the I60 blocks can self-assemble hydrophobically, thus leading to the mesoscale organization of these fibre-like HA structures *in situ* and generating ordered aggregates (Figure 3C). $(SN_A15)_3E50I60$ can therefore inhibit plate-like crystals and regulate fibre-like structure of HA.

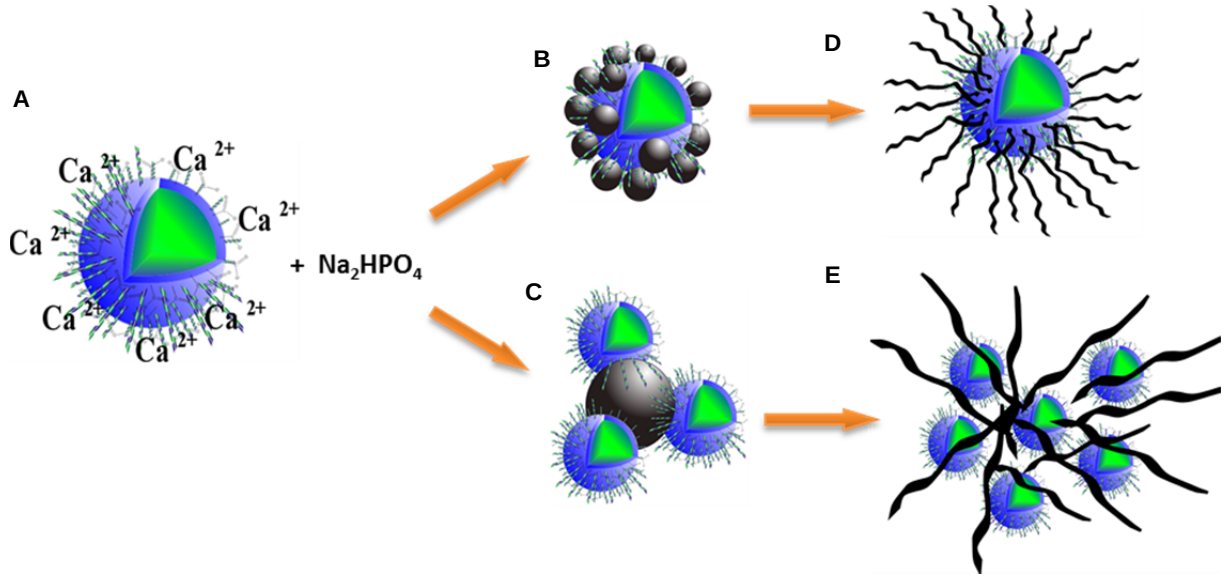

Figure 6. Schematic representation of the possible pathways the reaction mechanism can follow once phosphate solution is added to $(SN_A15)_3E50I60$ micelles dissolved in $CaCl_2$ solution. $(SN_A15)_3$ is represented by, whereas green and blue colors represent the I60 and E50 blocks, respectively. ACPs are represented by dark spheres.

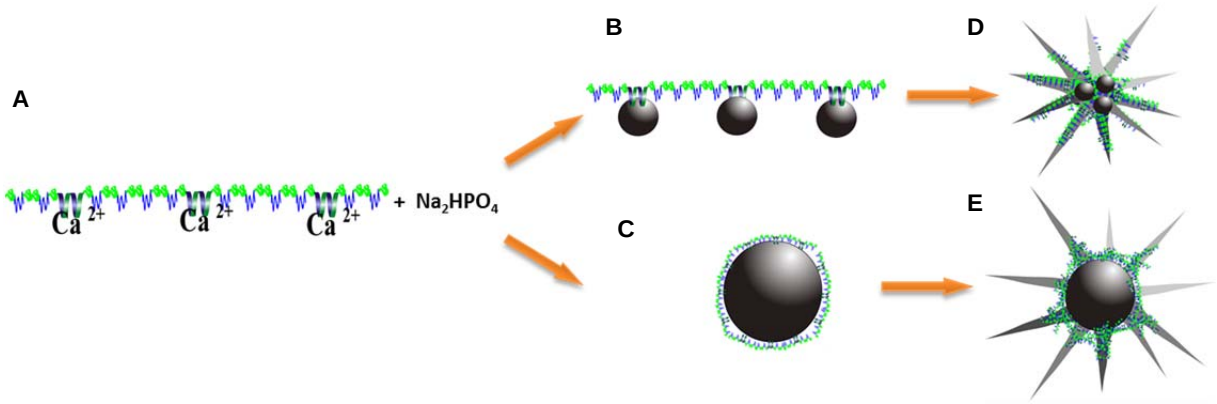

Figure 7. Schematic representation of the possible pathways the reaction mechanism can follow after addition of phosphate solution to a solution of ((IK)2-SN_A15-(IK)2)3 and calcium ions. SN_A15 is represented by, whereas green and blue color represent the (VPGIG) and (VPGKG) blocks, respectively. ACPs are represented by the dark spheres.

The hydrophilic (VPGKG) blocks in ((IK)2-SN_A15-(IK)2)3 are distributed amongst the hydrophobic (VPGIG) blocks. Although this ELR structure cannot form micelles in aqueous solution, calcium ions can accumulate on the SN_A15 moieties distributed along the monomer chain (Figure 7A). Upon addition of phosphate anions, there are also two possible pathways the reaction mechanism can follow, before I_t, to generate a ((IK)2-SN_A15-(IK)2)3/ACP hybrid structure. Firstly, the positive surface of SN_A15 (Figure 7A) can be screened by negative phosphate groups followed by additional calcium ions, etc., thus meaning that ACP could be formed (Figure 7B). In contrast, the hydrophobic segments ((VPGIG) block) tend to aggregate to minimize their surface area available to the solvent and become shielded from the hydration layer of kosmotropic ions.[36, 37] Secondly, ((IK)2-SN_A15-(IK)2)3 can adsorb to the ACP surfaces formed, once the phosphate solution is added, via SN_A15 (Figure 7C). In both possible pathways, the hydrophobic moieties can have a marked influence as regards to obstructing the transport of ions to ACP clusters[9, 35], thus preventing their flocculation bridging (Figure S7C) and inhibiting the transformation of ACP into a crystalline phase. The hydrophilic moieties are excluded from the hydrophobic one and can be separated when ((IK)2-SN_A15-(IK)2)3-mineral interactions become strong enough to disrupt and push aside. After I_t, a cooperative growth process gives rise to a high anisotropy of nano-hybrid filaments, thus generating the ((IK)2-SN_A15-(IK)2)3/ACP neuron-like morphology (Figures 5C, 5D, 7D, 7E). Moreover, the core of these neurons increases in size with ((IK)2-SN_A15-(IK)2)3 concentration because of the increasing number of hydrophobic moieties.

In light of the above, it can be suggested that, instead of transformation of ACP into a fibre-like HA, similar to the case of $(SN_A15)_3$E50I60, formation of an organic/inorganic hybrid material composed of amorphous micellar precursors is followed by a secondary nucleation of nano-hybrid filaments after I_t, similar to the case of ((IK)2-SN_A15-(IK)2)3).

The morphologies and phases of the generated calcium phosphate under control of the amphiphilic properties of ELRs in this work are in agreement with previous findings whereby the biomimetic mineralization process controlled by proteins tends to result in unfolded structures, e.g. random coils, due to their interaction motifs, rather than folded structures, e.g. β-turn, β-sheet, and α-helix.[10, 26] For example, the β-turn conformation found in $(SN_A15)_3$E50I60 is buried in the core of the micellar structure and, in consequence, has no control over calcium phosphate mineralization, whereas the random coils are included to guide SN_A15 during fibre-like HA formation. In contrast, the β-turn conformations found in (IK)2-SN_A15-(IK)2)3 are included to control the mineralization process that gives rise to organization of ACP/(IK)2-SN_A15-(IK)2)3 nanohybrid materials with a neuron-like structure. In other words, the secondary structure of polypeptides is associated with the hydration layer found around their monomer chains, with the random coils being more hydrated than the other secondary structures (β-turn, β-sheet, and α-helix) and playing an important role in ACP transformation.[10, 26, 38] This means that the third component of bone, namely water molecules, plays an important role in structuring and organizing apatite crystals, as demonstrated previously in the literature.[38]

Most of the works that have been published using ELRs in combination with the statherin domain have mainly focused on their synthesis[19, 20, 25] and *in vitro* behaviour.[12, 39-41] *In vitro* studies on ELR membranes with various epitopes and/or surface topographies have been conducted to assess their potential for dental and orthopaedic applications.[12, 39, 40] In addition, biomineralization experiments have also been performed on silk-like recombinamers (SS15m) combined with the carboxyl terminal domain of dentin matrix protein 1 (CDMP1), which is a well-known sequence reported to influence mineralization.[42] Besides those studies, up to now, there was no clear evidence on fundamental aspects such as the effect of statherin in the ELRs and how the

distribution of the statherin domain within the ELR backbone could affect biomineralization.

This study provides valuable information about the role of ELRs containing SN_A15, which could be used as multifunctional materials for various applications. For instance, their ability to control the mineralization process could allow them to be used to modulate bone mineral density and treat various bone diseases.[43-45] Thus, $(SN_A15)_3E50I60$ or ((IK)2-SN_A15-(IK)2)3 nanostructures could be used as drug nano-carriers for bone cancer treatments. In the case of $(SN_A15)_3E50I60$, hydrophobic drugs could be carried by its hydrophobic core of I60 blocks, whereas the hydrophilic block $(SN_A15)_3E50$ could be used to control the mineralization process. Moreover, as ((IK)2-SN_A15-(IK)2)3 controls the formation of neuron-like hybrid structures, it could interact with hydrophilic drugs to form organized nanostructures. In addition, ((IK)2-SN_A15-(IK)2)3 could be used to stabilize labile/metastable phases and form a neuron-like structure, and the resulting filaments could be used to impart topographical and even biological cues to trigger various cellular events. For example, they could be introduced as a complementary component in an extracellular matrix to induce the ingrowth of vascular and bone-forming cells.[46, 47]

Conclusions

The control of calcium phosphate nanostructures formations by the hybrid elastin-like-statherin recombinamers $(SN_A15)_3E50I60$ and ((IK)2-SN_A15-(IK)2)3 depends on two main parameters. Firstly, it depends on the presence of a high local charge on their surface that can delay the I_t. $(SN_A15)_3E50I60$ can delay the secondary precipitation of calcium phosphate with a constant I_t at increasing concentration, whereas ((IK)2-SN_A15-(IK)2)3 can delay secondary precipitation with a steady concentration-dependent increase in I_t. These striking differences in the effects of ELRs on I_t have been interpreted as being dependent on the second main parameter, namely the amphiphilic properties of ELRs. Thus, $(SN_A15)_3E50I60$ can self-assemble to form nanoparticles in which the $(SN_A15)_3$ domains are exposed on the outer surface. This means that the $(SN_A15)_3E50$ block can control the transformation of ACP into a fibre-like HA structure, whereas the I60 blocks can self-assemble hydrophobically, thus leading to the mesoscale organization of these fibre-like HA structures *in situ* and generating ordered aggregates. In contrast, the hydrophilic (VPGKG) blocks are distributed amongst the hydrophobic (VPGIG) blocks in ((IK)2-SN_A15-(IK)2)3, thus hindering the transformation of ACP into a crystalline phase. In this case, a neuron-like morphology of ((IK)2-SN_A15-(IK)2)3/ACP with high anisotropy nano-hybrid filaments is generated. In conclusion, the amphiphilic properties of thermally-sensitive amphiphilic elastin-like multiblock recombinamers play an important role in tuning the SN_A15 bioactive domain and, in consequence, the calcium phosphate morphologies generated.

Acknowledgements

Authors acknowledge financial supported by the European Commission Seventh Framework Programme through InnovaBone Project (NMP3-LA-2011-263363; HEALTH-F4-2011-278557), the Spanish Minister of Economy and Competitivity (MAT2012-38043-C02-01; MAT2012-38438-C03; MAT2013 -41723-R; MAT2013 -42473-R) co-funded by the EU through European Regional Development Funds, support for the research of MPG was received through the "ICREA Academia" award for excellence in research, and funded by the Generalitat de Catalunya, and projects funded by the Regional Government of Castilla y León: VA244U13; VA313U14.

Notes and References

The authors declare no competing financial interest.

1. J. D. Hartgerink, E. Beniash and S. I. Stupp, *Science*, 2001, **294**, 1684-1688.
2. H. Cölfen and S. Mann, *Angewandte Chemie International Edition*, 2003, **42**, 2350-2365.
3. M. H. Misbah, L. Quintanilla, M. Alonso and J. C. Rodríguez-Cabello, *Polymer*, 2015, **81**, 37-44.
4. R.-Q. Song and H. Cölfen, *CrystEngComm*, 2011, **13**, 1249-1276.
5. M. Antonietti, M. Breulmann, C. G. Göltner, H. Cölfen, K. K. W. Wong, D. Walsh and S. Mann, *Chemistry – A European Journal*, 1998, **4**, 2493-2500.
6. W. Tjandra, P. Ravi, J. Yao and K. C. Tam, *Nanotechnology*, 2006, **17**, 5988-5994.
7. D. Hentrich, M. Junginger, M. Bruns, H. G. Börner, J. Brandt, G. Brezesinski and A. Taubert, *CrystEngComm*, 2015, **17**, 6901-6913.
8. B. J. Tarasevich, C. C. Chusuei and D. L. Allara, *The Journal of Physical Chemistry B*, 2003, **107**, 10367-10377.
9. M. Espanol, Z. T. Zhao, J. Almunia and M.-P. Ginebra, *Journal of Materials Chemistry B*, 2014, **2**, 2020-2029.
10. P. Kašparová, M. Antonietti and H. Cölfen, *Colloids and Surfaces A: Physicochemical and Engineering Aspects*, 2004, **250**, 153-162.
11. Z. A. Schnepp, R. Gonzalez-McQuire and S. Mann, *Advanced Materials*, 2006, **18**, 1869-1872.
12. E. Tejeda-Montes, A. Klymov, M. R. Nejadnik, M. Alonso, J. C. Rodriguez-Cabello, X. F. Walboomers and A. Mata, *Biomaterials*, 2014, **35**, 8339-8347.
13. D. W. Urry, *Progress in Biophysics and Molecular Biology*, 1992, **57**, 23-57.
14. D. Urry, *J Protein Chem*, 1988, **7**, 1-34.
15. J. C. Rodríguez-Cabello, M. Alonso, T. Pérez and M. M. Herguedas, *Biopolymers*, 2000, **54**, 282-288.
16. D. W. Urry, *The Journal of Physical Chemistry B*, 1997, **101**, 11007-11028.

17. T. Yamaoka, T. Tamura, Y. Seto, T. Tada, S. Kunugi and D. A. Tirrell, *Biomacromolecules*, 2003, **4**, 1680-1685.
18. A. Girotti, J. Reguera, F. J. Arias, M. Alonso, A. M. Testera and J. C. Rodríguez-Cabello, *Macromolecules*, 2004, **37**, 3396-3400.
19. C. García-Arévalo, M. Pierna, A. Girotti, F. J. Arias and J. C. Rodríguez-Cabello, *Soft Matter*, 2012, **8**, 3239-3249.
20. C. García-Arévalo, J. F. Bermejo-Martín, L. Rico, V. Iglesias, L. Martín, J. C. Rodríguez-Cabello and F. J. Arias, *Molecular Pharmaceutics*, 2013, **10**, 586-597.
21. P. A. Raj, M. Johnsson, M. J. Levine and G. H. Nancollas, *Journal of Biological Chemistry*, 1992, **267**, 5968-5976.
22. J. Rodríguez-Cabello, A. Girotti, A. Ribeiro and F. Arias, in *Nanotechnology in Regenerative Medicine*, eds. M. Navarro and J. A. Planell, Humana Press, 2012, vol. 811, ch. 2, pp. 17-38.
23. J. Henderson, R. D. Ricker, B. A. Bidlingmeyer and C. Woodward, *Amino acid analysis using Zorbax Eclipse-AAA columns and the Agilent*, 2000, **1100**, 1-10.
24. T. Tsuji, K. Onuma, A. Yamamoto, M. Iijima and K. Shiba, *Proceedings of the National Academy of Sciences*, 2008, **105**, 16866-16870.
25. J. S. Barbosa, A. Ribeiro, A. M. Testera, M. Alonso, F. J. Arias, J. C. Rodríguez-Cabello and J. F. Mano, *Advanced Engineering Materials*, 2010, **12**, B37-B44.
26. J. S. Evans, *Current opinion in colloid & interface science*, 2003, **8**, 48-54.
27. S. W. Provencher and J. Gloeckner, *Biochemistry*, 1981, **20**, 33-37.
28. A. J. Adler, N. J. Greenfield and G. D. Fasman, *Methods in enzymology*, 1972, **27**, 675-735.
29. C. Nicolini, R. Ravindra, B. Ludolph and R. Winter, *Biophysical journal*, 2004, **86**, 1385-1392.
30. H. Reiersen, A. R. Clarke and A. R. Rees, *Journal of Molecular Biology*, 1998, **283**, 255-264.
31. S. Raynaud, E. Champion, D. Bernache-Assollant and P. Thomas, *Biomaterials*, 2002, **23**, 1065-1072.
32. K. Lin, C. Wu and J. Chang, *Acta biomaterialia*, 2014, **10**, 4071-4102.
33. M. Sadat-Shojai, M.-T. Khorasani, E. Dinpanah-Khoshdargi and A. Jamshidi, *Acta biomaterialia*, 2013, **9**, 7591-7621.
34. A.-W. Xu, Y. Ma and H. Cölfen, *Journal of Materials Chemistry*, 2007, **17**, 415-449.
35. S. Mann, *Angewandte Chemie International Edition*, 2000, **39**, 3392-3406.
36. J. M. Peula-García, J. L. Ortega-Vinuesa and D. Bastos-González, *The Journal of Physical Chemistry C*, 2010, **114**, 11133-11139.
37. P. Lo Nostro and B. W. Ninham, *Chemical reviews*, 2012, **112**, 2286-2322.
38. Y. Wang, S. Von Euw, F. M. Fernandes, S. Cassaignon, M. Selmane, G. Laurent, G. Pehau-Arnaudet, C. Coelho, L. Bonhomme-Coury and M.-M. Giraud-Guille, *Nature materials*, 2013, **12**, 1144-1153.
39. Y. Li, X. Chen, A. J. Ribeiro, E. D. Jensen, K. V. Holmberg, J. C. Rodriguez-Cabello and C. Aparicio, *Advanced Healthcare Materials*, 2014, **3**, 1638-1647.
40. E. Tejeda-Montes, K. H. Smith, E. Rebollo, R. Gómez, M. Alonso, J. C. Rodriguez-Cabello, E. Engel and A. Mata, *Acta biomaterialia*, 2014, **10**, 134-141.
41. S. Prieto, A. Shkilnyy, C. Rumplasch, A. Ribeiro, F. J. Arias, J. C. Rodríguez-Cabello and A. Taubert, *Biomacromolecules*, 2011, **12**, 1480-1486.
42. J. Huang, C. Wong, A. George and D. L. Kaplan, *Biomaterials*, 2007, **28**, 2358-2367.
43. X. Bi, J. A. Sterling, A. R. Merkel, D. S. Perrien, J. S. Nyman and A. Mahadevan-Jansen, *Bone*, 2013, **56**, 454-460.
44. K. A. Fitzgerald, J. Guo, E. G. Tierney, C. M. Curtin, M. Malhotra, R. Darcy, F. J. O'Brien and C. M. O'Driscoll, *Biomaterials*, 2015, **66**, 53-66.
45. E. M. Alexandrino, S. Ritz, F. Marsico, G. Baier, V. Mailänder, K. Landfester and F. R. Wurm, *Journal of Materials Chemistry B*, 2014, **2**, 1298-1306.
46. A. I. Hoch, V. Mittal, D. Mitra, N. Vollmer, C. A. Zikry and J. K. Leach, *Biomaterials*, 2016, **74**, 178-187.
47. A. D. Berendsen and B. R. Olsen, *Journal of internal medicine*, 2015, **277**, 674-680.